

Measurements of Tip Vortices from a Full-Scale UH-60A Rotor by Retro-Reflective Background Oriented Schlieren and Stereo Photogrammetry

Edward T. Schairer
edward.t.schairer@nasa.gov
 Aerospace Engineer
 NASA Ames Research Center
 Moffett Field, CA, USA

Laura K. Kushner
laura.k.kushner@nasa.gov
 Research Engineer
 Aerospace Computing, Inc.
 Moffett Field, CA, USA

James T. Heineck
james.t.heineck@nasa.gov
 Photographic Technologist
 NASA Ames Research Center
 Moffett Field, CA, USA

ABSTRACT

Positions of vortices shed by a full-scale UH-60A rotor in forward flight were measured during a test in the National Full-Scale Aerodynamics Complex at NASA Ames Research Center. Vortices in a region near the tip of the advancing blade were visualized from two directions by Retro-Reflective Background-Oriented Schlieren (RBOS). Correspondence of points on the vortex in the RBOS images from both cameras was established using epipolar geometry. The object-space coordinates of the vortices were then calculated from the image-plane coordinates using stereo photogrammetry. One vortex from the tip of the blade that had most recently passed was visible in most of the data. The visibility of the vortices was greatest at high thrust and low advance ratios. At these favorable conditions, vortices from the most recent passages of all four blades were detected. The vortex positions were in good agreement with PIV data for a case where PIV measurements were also made. RBOS and photogrammetry provided measurements of the angle at which each vortex passed through the PIV plane.

NOTATION

| | |
|------------|--|
| C_T | Thrust coefficient |
| DLT | Direct Linear Transformation |
| e | Epipole |
| f | Lens focal length (mm) |
| F | Fundamental Matrix of epipolar geometry |
| L_{1-11} | Direct Linear Transformation coefficients |
| M_{tip} | Mach number at blade tip due to rotation |
| n | Number of targets |
| O | Perspective center of camera |
| PIV | Particle Image Velocimetry |
| r | Radial distance from rotor axis |
| R | Rotor radius |
| RBOS | Retro-reflective Background Oriented Schlieren |
| ROI | Region of interest |
| x, y, z | Streamwise, spanwise, and vertical space coordinates |
| Δy | Speckle object-space displacement |
| z_{bg} | Distance from density disturbance to BOS background |
| z_{cam} | Distance from density disturbance to BOS camera |
| X, Y | Horizontal, vertical image-plane coordinates (pixels) |
| α | Rotor shaft angle, deg |
| ϵ | Deflection angle of light due to density gradient (deg) |
| ϕ | Vortex angle projected onto x - z plane, positive up (deg) |

| | |
|----------|---|
| σ | Rotor solidity |
| μ | Advance ratio (free-stream velocity/ V_{tip}) |
| θ | Vortex angle projected onto x - y plane, positive to port (deg) |
| ψ | Rotor azimuth angle (0 when blade 1 is fully aft) (deg) |

Subscripts

| | |
|-----|-----------------|
| A | Sidewall camera |
| B | Ceiling camera |
| Tip | Rotor tip |

INTRODUCTION

A full-scale UH-60A helicopter rotor was tested on the Large Rotor Test Apparatus (LRTA) in the National Full-Scale Aerodynamic Complex (NFAC) at NASA Ames Research Center (Ref. 1). One objective of this test was to measure the response of the rotor over a range of test conditions and rotor control settings. Quantities of interest

Presented at the AHS 69th Annual Forum, Phoenix, Arizona, May 21–23, 2013. This is a work of the U.S. government and is not subject to copyright protection in the U.S.

included displacement of the rotor blades, unsteady pressure distributions on the blades, and flow conditions in the region near the advancing blade. Blade displacements were measured by an eight-camera stereo photogrammetry system (Ref. 2, 3). Two blades were instrumented, one with unsteady pressure transducers, and the other with strain gauges and accelerometers. The flow near the advancing blade was measured by two techniques: Particle Image Velocimetry (PIV) was used to measure flow velocities in a vertical plane at the streamwise station of the advancing blade (Refs. 4, 5); and RBOS and stereo photogrammetry were used to visualize vortices and measure their spatial coordinates as the vortices passed through the PIV plane. Knowing the angle at which the vortices passed through the PIV measurement plane allows greater accuracy in computing vortex strength and core diameters from the PIV measurements.

Vortices shed from rotors and fixed-wing aircraft have been successfully measured in a variety of tests. Nearly 25 years ago retro-reflective shadowgraphy was shown to be an effective means of visualizing vortices in both small-scale and large-scale applications (Refs. 8–15). Shadowgraphy is attractive because it provides instantaneous visualizations of the flow over a very wide field of view. Typically, shadowgraphy measurements have been based on images acquired by cameras in the rotor plane or aligned with the axis of rotation, and the transformation from image to object space has been accomplished by a simple scaling using a reference object of known size in the field of view (Ref. 10).

Another method for visualizing tip vortices is to inject smoke from the tip of the rotor or wing. In rotor applications, smoke tends to quickly diffuse limiting visibility to early wake ages, and hardware required to introduce the smoke can be intrusive. Meyn and Bennett (Ref. 16) used smoke to visualize vortices from a fixed-wing aircraft in tests in the 40- by 80-Ft Wind Tunnel at NASA Ames. In addition, they employed two cameras and rigorous stereo photogrammetry rather than simplistic scaling to determine the space coordinates of the vortex filaments. Stereo photogrammetry not only improves accuracy but also allows greater flexibility in placing cameras.

More recently, BOS and RBOS have been used to visualize vortices from helicopters (Ref.17). RBOS is closely related to retro-reflective shadowgraphy. Both methods make use of a camera, a light source that is co-located with the camera, and a retro-reflective screen or background against which the region of interest is observed. BOS and RBOS have the advantage of providing quantitative measures of the angular deviation of light from the density disturbance. Under conditions where simplifying assumptions are valid, these measurements can be used to infer density (Ref. 18). In addition, RBOS post-processing allows rotating a virtual knife-edge to highlight density gradients in a chosen direction. Because of these advantages, RBOS was chosen to visualize vortices in the UH-60A tests.

A prototype of the RBOS/photogrammetry system (Ref. 6) was demonstrated during the Individual Blade Control (IBC) test of the UH-60A rotor conducted in Spring 2009 (Ref. 7) in the NFAC 40- by 80-Wind Tunnel. RBOS was successfully used to visualize vortices in the region near the advancing blade using two cameras mounted in a window in the opposite sidewall. However, because the cameras were on the opposite side of the test section as the region of interest (ROI) and were only slightly above the rotor plane, they sometimes viewed the ROI through vortices that were shed by the much-closer retreating blade. These nearside vortices obscured vortices in the ROI. Another shortcoming of the photogrammetry system used for the IBC test was that the separation between the cameras was too small to allow meaningful stereo measurements. The IBC test also revealed that improvements could be made to the hardware used to calibrate the cameras.

For the present test, known as the Airloads Wind Tunnel Test (Ref. 1) and conducted in Spring 2010, the RBOS/photogrammetry system was redesigned to mitigate these problems. Both cameras were located well above the rotor plane to avoid lines-of-sight through the nearside, retreating-blade vortices. In addition, there was much greater separation between the cameras, which yielded differences in perspective sufficient to allow 3D measurements. A new calibration structure that was more rigid and easier to install was designed and used in this test.

This report describes the RBOS/photogrammetry system that was used in the UH-60A Airloads test and presents typical results of the measurements.

APPROACH

The first step in measuring the spatial positions of the vortex filaments was to use RBOS to visualize the vortices in the images from both cameras. Then, points that lay along each filament were identified in the RBOS data computed from each image. Epipolar geometry was used to match points in the images from both cameras that corresponded to the same physical point in space. Finally, stereo photogrammetry was used to compute the space coordinates of each pair of corresponding points.

Retro-Reflective Background-Oriented Schlieren

Retro-reflective Background Oriented Schlieren (RBOS, Refs. 19, 20) measures density gradients in a medium. A speckle pattern on a retro-reflective background behind a region of interest (ROI) is imaged in quiescent, wind-off conditions and at wind-on test conditions. When a vortex filament lies in the ROI, the density gradient in the vortex core causes the speckled background in the neighborhood of the vortex to shift toward the core, in the direction of the decreasing density. This characteristic makes it possible to precisely locate vortices in the RBOS images.

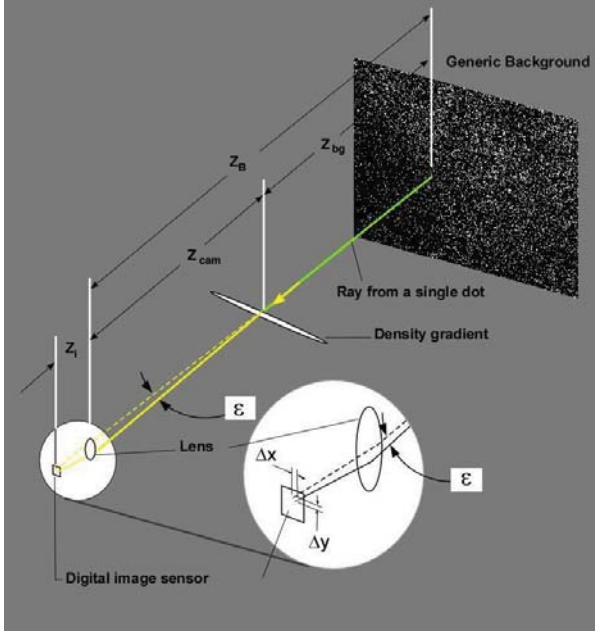


Figure 1. RBOS geometry.

The magnitude of the speckle displacements in the image plane (Δy) is given by (Ref. 19):

$$\Delta y = f \times \frac{z_{bg}}{z_{bg} + z_{cam} - f} \times \varepsilon \quad (1)$$

where f is the lens focal length, z_{cam} and z_{bg} are the distances from the density gradient to the camera and background, respectively, and ε is the angular deflection of a light ray from the background to the camera produced by the density gradient (Figure 1).

Increasing the focal length of the lens increases the pixel displacements, but at the cost of a more limited field of view. Pixel displacements can also be increased by increasing the distance between the ROI and the background (z_{bg}) if the camera-to-ROI distance (z_{cam}) is fixed. An undesirable side-effect of increasing z_{bg} , however, is that the contrast of the image will decrease making accurate measurement of pixel displacements more difficult. This occurs because the distance between the focal planes for the background and the ROI increases as their separation in space increases. This effect can be reduced by stopping down the lens to increase the depth of field, but at the cost of either decreased image brightness or longer exposures. Another way to increase pixel displacements is to move the camera closer to the ROI while holding z_{bg} fixed.

In most practical wind-tunnel applications of BOS, z_{cam} and z_{bg} are severely constrained by the position of the ROI in the test section and by where cameras and backgrounds may be installed: cameras usually are located in windows and backgrounds are usually applied to the test-section wall. Therefore, choice of lens focal length is often the only

practical way of affecting pixel displacements, and this becomes a trade-off between larger displacements and more limited field of view.

Speckle shifts in the background are measured in the same way as particle displacements are measured in Particle Image Velocimetry (PIV) images (Ref. 21): points of interest in the images are defined by a rectangular grid, and the local image-plane displacement at each node of the grid is measured by cross correlating the wind-off and wind-on images in a small (e.g., 20 x 20 pixels) interrogation window centered on the node.

With both RBOS and retro-reflective shadowgraphy, a retroreflective background is used to maximize the light reflected from the background. This increases the contrast between the dark speckles or shadows and bright background, improving the signal-to-noise ratio (SNR), thus allowing shorter integration times that can freeze flow unsteadiness. The only optical access that is needed is a small window that can accommodate both the camera and the light source. This allows RBOS or retroreflective shadowgraphy to provide schlieren or shadowgraph data in wind tunnels that lack large, expensive, schlieren-quality windows. Though RBOS cannot currently provide real-time data, as does retroreflective shadowgraphy, post-processing the images allows for insertion of a virtual knife edge that can be oriented horizontally, vertically or any angle in between, thus optimizing each data point for the given flow condition or to highlight various features.

Stereo Photogrammetry

Stereo photogrammetry (Ref. 22, 23) measures the positions of points in a region of interest from images acquired from at least two directions. The object-space coordinates of any point in the ROI that appears in both images can be computed from the image-plane coordinates of the point in both images and the camera calibration coefficients. The cameras can be calibrated in situ by placing a calibration object with targets of known spatial positions in the ROI and imaging it with both cameras. The sensitivity of the measurement in the direction perpendicular to the baseline between the cameras is greatest when the angular separation between the cameras is 90°.

The transformation between image- and object-space coordinates is based on a pin-hole representation of a camera. The image plane is perpendicular to the optical axis and is displaced from the pinhole (lens) by the effective lens focal length. Each point in space is projected through the pinhole onto the image plane along a straight line. For a target i , this colinearity geometry can be approximated by the Direct Linear Transformation (DLT, Ref. 24):

$$X_i = \frac{L_1 x_i + L_2 y_i + L_3 z_i + L_4}{L_9 x_i + L_{10} y_i + L_{11} z_i + 1} \quad (2)$$

$$Y_i = \frac{L_5 x_i + L_6 y_i + L_7 z_i + L_8}{L_9 x_i + L_{10} y_i + L_{11} z_i + 1}$$

where (X_i, Y_i) are the image-plane coordinates, (x_i, y_i, z_i) are the object-space coordinates and L_{1-11} are calibration coefficients. The equations for n calibration targets whose image- and object-space coordinates are known may be written as an $n \times 11$ set of linear equations:

$$\begin{bmatrix} x_1 & y_1 & z_1 & 1 & 0 & 0 & 0 & 0 & X_1 x_1 & X_1 y_1 & X_1 z_1 \\ x_2 & y_2 & z_2 & 1 & 0 & 0 & 0 & 0 & X_2 x_2 & X_2 y_2 & X_2 z_2 \\ \vdots & \vdots & \vdots & \vdots & \vdots & \vdots & \vdots & \vdots & \vdots & \vdots & \vdots \\ x_n & y_n & z_n & 1 & 0 & 0 & 0 & 0 & X_n x_n & X_n y_n & X_n z_n \\ 0 & 0 & 0 & 0 & x_1 & y_1 & z_1 & 1 & Y_1 x_1 & Y_1 y_1 & Y_1 z_1 \\ 0 & 0 & 0 & 0 & x_2 & y_2 & z_2 & 1 & Y_2 x_2 & Y_2 y_2 & Y_2 z_2 \\ \vdots & \vdots & \vdots & \vdots & \vdots & \vdots & \vdots & \vdots & \vdots & \vdots & \vdots \\ 0 & 0 & 0 & 0 & x_n & y_n & z_n & 1 & Y_n x_n & Y_n y_n & Y_n z_n \end{bmatrix} \times \begin{bmatrix} L_1 \\ L_2 \\ L_3 \\ L_4 \\ L_5 \\ L_6 \\ L_7 \\ L_8 \\ L_9 \\ L_{10} \\ L_{11} \end{bmatrix} = - \begin{bmatrix} X_1 \\ X_2 \\ \vdots \\ X_n \\ Y_1 \\ Y_2 \\ \vdots \\ Y_n \end{bmatrix} \quad (3)$$

If there are 6 or more targets, the set of equations is over-determined and can be solved by linear least squares for the calibration coefficients L_{1-11} . Equation 2 is generally ill-conditioned and thus must be solved by singular value decomposition (Ref. 25).

Once the calibration coefficients for at least two cameras, A and B , have been determined, the object-space coordinates of an unknown point (x_i, y_i, z_i) that is imaged by both cameras may be computed from the image-plane coordinates of the point in both images $(X_i^A, Y_i^A), (X_i^B, Y_i^B)$ and the camera calibration coefficients (L_{1-11}^A, L_{1-11}^B) :

$$\begin{bmatrix} L_1^A + X_i^A L_9^A & L_2^A + X_i^A L_{10}^A & L_3^A + X_i^A L_{11}^A \\ L_5^A + Y_i^A L_9^A & L_6^A + Y_i^A L_{10}^A & L_7^A + Y_i^A L_{11}^A \\ L_1^B + X_i^B L_9^B & L_2^B + X_i^B L_{10}^B & L_3^B + X_i^B L_{11}^B \\ L_5^B + Y_i^B L_9^B & L_6^B + Y_i^B L_{10}^B & L_7^B + Y_i^B L_{11}^B \end{bmatrix} \times \begin{bmatrix} x_i \\ y_i \\ z_i \end{bmatrix} = \begin{bmatrix} L_4^A + X_i^A \\ L_8^A + Y_i^A \\ L_4^B + X_i^B \\ L_8^B + Y_i^B \end{bmatrix} \quad (4)$$

Equation 4 is also an over-determined set of linear equations that is solved for (x_i, y_i, z_i) using the least-squares method.

In the present test, the object-space coordinates of the calibration targets were not precisely known because the structure on which they were placed (described below) was large and could not be built to exacting tolerances without being excessively expensive. Therefore, an iterative

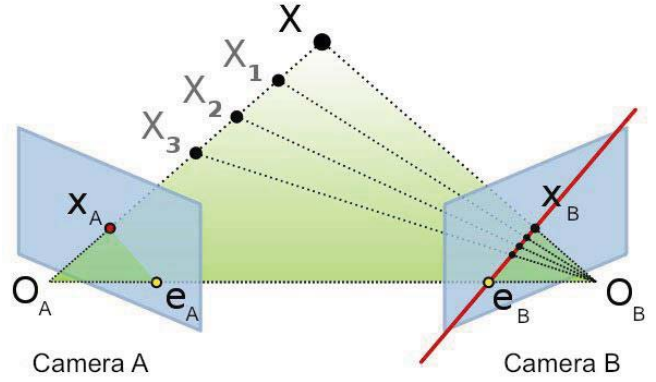


Figure 2. Epipolar geometry (Ref. 28). Points O_A and O_B are the optical centers of cameras A and B . e_A and e_B are the epipoles in images A and B . Line $e_B X_B$ is the epipolar line corresponding to point X_A .

calibration procedure, or bundle adjustment, was used that refined the space coordinates of the targets at each pass by minimizing the re-projection error (the root-mean-square of the differences between the measured target coordinates in both cameras and the theoretical coordinates computed from Eq. 4). This was done using Levenberg-Marquardt non-linear, least-squares optimization (Ref. 26). Bundle adjustment couples the calibrations of the two cameras. Without this adjustment the calibrations are independent.

Epipolar Geometry

One of the requirements of stereo photogrammetry is that measurement points in the images of both cameras must correspond to the same physical point in space. In many applications of photogrammetry, particularly those that use targets, this correspondence is self-evident. In the present test, however, where there were no targets and the vortices were invisible, epipolar geometry (Ref. 27) was used to establish correspondence between points on the vortex in the images of both cameras. This approach is very similar to that employed by Meyn and Bennett (Ref. 16), who measured the positions of vortices shed by a fighter aircraft in the 40- by 80-ft Wind Tunnel. The principal difference between the approach of Ref. 16 and the present study was the method of visualizing the vortices (smoke released from the wingtips versus RBOS).

Epipolar geometry is also based on the pinhole representation of a camera and exploits the idea that a point in the image (X_A in Fig. 1, Ref. 28) from one camera (A) is mapped to an epipolar line (line $e_B X_B$ in Fig. 2) in the image of a second camera (B), and visa versa. Therefore, if an object-space point, x , can be located in image A then the same (corresponding) point in image B must lie on the epipolar line $e_B X_B$. In other words, each epipolar line is the image of the ray that passes from the perspective center (i.e., pinhole) of the second camera through the point in space that is imaged by the first camera. It follows that all epipolar

lines pass through a common point known as the epipole (e_B and e_A), which is the image of the perspective center (O_A , O_B) of one camera in the image of the other camera. Thus all epipolar lines converge at the epipole.

The epipolar constraint can be described by the equation:

$$\begin{bmatrix} X_A & Y_A & 1 \end{bmatrix} \times F \times \begin{bmatrix} X_B \\ Y_B \\ 1 \end{bmatrix} = 0 \quad (5)$$

where (X_A, Y_A) and (X_B, Y_B) are corresponding points in images A and B , respectively, and F is a singular 3×3 matrix known as the Fundamental Matrix. The Fundamental Matrix has seven degrees of freedom and thus may be computed from the image-plane coordinates of seven or more points that appear in both images. The same images and targets that are used to compute the DLT calibrations may also be used to compute the Fundamental Matrix. Unlike the DLT, however, the space coordinates of the targets do not enter into the calculation of the Fundamental Matrix. The method used in the present test to compute the Fundamental Matrix was the eight-point algorithm described by Hartley (Ref. 29).

Epipolar geometry restricts the search for corresponding points to a line. Additional information is required to establish where on the line the corresponding point lies. In the present case, this information is provided by the image of the vortex filaments as visualized by RBOS. A point that lies on the filament in image A must also lie on the filament in image B . Therefore, the point in image B that corresponds to a point on the filament in image A is the intersection in image B of the epipolar line and the vortex filament. Ideally the epipolar lines would be perpendicular to the vortex filaments to minimize the uncertainty in computing their intersection. In the present test, where the vortex filaments were nearly horizontal, it was important for the cameras to have predominately vertical separation because this would result in epipolar lines in the images with a significant vertical component.

WIND TUNNEL AND TEST ARTICLE

The 40- by 80-Foot Wind Tunnel is a closed-return, atmospheric wind tunnel located at NASA Ames Research Center and operated by Arnold Engineering Development Center. The test section is 80 feet long and has a cross section that is oval: the ceiling and floor are flat and 40 feet wide and the sidewalls are semicircular with radii of 20 feet. An acoustic liner decreases the actual dimensions to 39 x 79 ft. The upper half of the test section is formed by hinged, “clam-shell” doors that open to allow test articles and other large or heavy objects to be hoisted into the test section by an overhead crane. The tunnel is driven by six 40-ft diameter fans each of which is turned by a 22,500-HP electric motor. Maximum airspeed in the test section is 300 kts.



Figure 3. LRTA and UH-60A rotor installed in 40- by 80-Foot Wind Tunnel. View is from upstream, port quadrant.

The test article was a full-scale flight rotor from a UH-60A helicopter (Ref. 7). The rotor had four blades and a radius (R) of 26.83 ft. Each blade was twisted -18° and had a chord of 20.76 in. The tip of each blade was swept back 20° . The geometric solidity ratio (σ) was 0.0826, and 100% RPM was 258. One blade was instrumented with 242 pressure transducers and another was instrumented with strain gauges. An instrumentation “hat” was mounted on top of the UH-60A hub.

The rotor was supported by the Large Rotor Test Apparatus (LRTA). The drive system of this apparatus was powered by two 3000-HP motors. The LRTA was mounted on three struts that allowed angle-of-attack (α) changes of $\pm 15^\circ$. The height of the rotor plane at $\alpha = 0^\circ$ was 9.5 inches above the tunnel centerline and 20.3 ft above the acoustic liner on the test-section floor. Figure 3 shows the rotor and LRTA installed in the test section.

RBOS AND PHOTOGRAMMETRY SYSTEM

Layout and Design

The challenge in designing the photogrammetry system was to find two positions suitable for mounting cameras and lamps that provided sufficient separation for stereo measurements and provided sightlines to the ROI that did not pass through vortices produced by the retreating blades. The separation between cameras needed to be mostly vertical so that the epipolar lines would also be vertical and nearly perpendicular to the horizontal vortices. Finally, acoustic panels in the background of the ROI as seen by each camera required covering with retro-reflective material, and the viewing angle of the retro-reflective panels could not exceed $15\text{-}20^\circ$ without significant loss in light returned to the camera. Due to cost and time constraints and to minimize degradation of the acoustic liner, the number of acoustic panels covered with retro-reflective material was limited. Therefore, having as much overlap of the backgrounds for

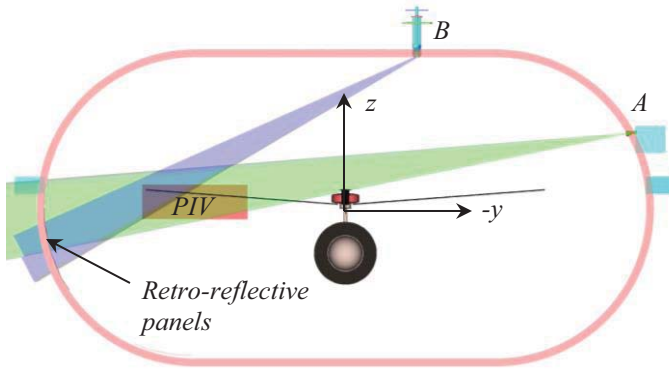


Figure 4. Schematic view from upstream showing PIV region and fields of view of RBOS cameras.

the two cameras as possible was desirable. For ease of installation, the background panels also had to be accessible (i.e., not in the ceiling or very high in the sidewalls) and could not be in a high-traffic area (e.g., on the floor of the test section).

The RBOS region of interest was just downstream of the advancing blade. The ROI extended from about $r/R = 0.75$ to just beyond the rotor tip and included the outboard part of the PIV measurement region, which lay in the cross-stream vertical plane that passed through the trailing edge of the swept tip when the blade was at $\psi = 90^\circ$ (Ref. 5).

A PIV window in the port sidewall just abeam the rotor mast and above the tunnel centerline was suitable for mounting one camera. The line-of-sight from this location to the ROI passed directly over the instrumentation hat on top of the rotor hub. Although there were no properly situated windows for the second camera, there were light-fixtures in the ceiling of the test section whose housings could accommodate a camera if the lamp were removed. Therefore, the second camera was located in one of these light-fixture housings slightly downstream of the sidewall camera and on the port side of the tunnel centerline. From these positions, the angular separation between the lines-of-sight of the two cameras was about 20° , and there was significant vertical separation between them. Figures 4 and 5 are schematic views that show the intersection of the camera fields of view in the region of interest. Figure 4 also shows the PIV region.

Virtual imaging (Refs. 30, 31) was used to predict the view of each camera and to identify acoustic panels that lay in the background of the ROI. This was particularly important for the ceiling-mounted camera (B) because its position—at the bottom of the lamp housing, which was 5 feet deep, 11.5 inches in diameter and 40 ft above the floor of the test section—was completely inaccessible, making direct visual observation from this position almost impossible. In addition, because of the confined space of the lamp housing and the oblique view to the ROI, the optical

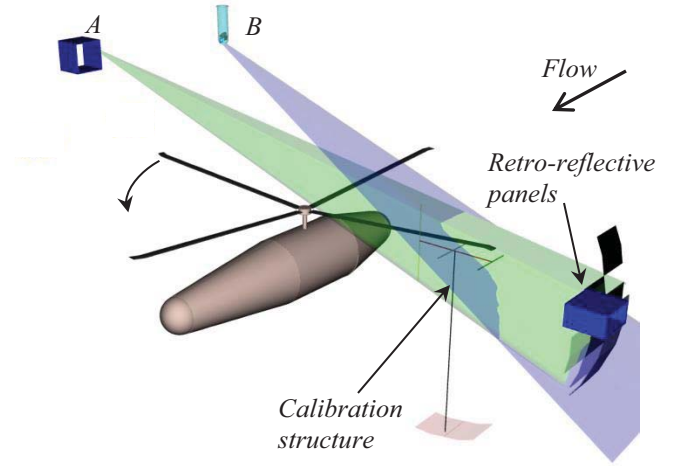


Figure 5. Isometric view from downstream showing rotor and fields of view of RBOS cameras. Calibration structure and retro-reflective panels are to the right. Tunnel walls are not shown.

path was folded within the housing. This was accomplished with two mirrors, forming a periscope (Fig. 6). Predicting the view of the camera mounted in the portside PIV window (A) was much simpler because the ROI was viewed directly.

The lens focal lengths were chosen to fill the camera fields of view with the region of interest and the speckled acoustic panels that lay in the background. The sidewall camera (A) was fitted with a 300-mm lens and the ceiling camera (B) with a 200-mm lens. With these lenses the spatial resolutions of the cameras at the tip of the advancing blade were both approximately 1.6 pixels/mm. Eight acoustic panels were covered with retro-reflective plates.

Cameras and Lamps

The ROI was imaged by two Redlake EC11000 digital cameras. The sensor for these cameras had 4008×2672 pixels with 9- μm pitch and 12-bit dynamic range. The cameras were controlled via a rack-mounted PC with stream-to-disk capabilities.

Illumination was provided by two custom-built, high-intensity red LED flash-lamps (Ref. 32), one co-located with each camera. Each lamp was composed of 18 individual elements that were distributed around a circular opening through which the lens protruded, forming a ring lamp. Placing the light sources as close to the camera lenses as possible was necessary to take maximum advantage of the retro-reflective properties of the background.

The sidewall camera and lamp were mounted on optical posts in a small compartment behind the PIV window opening. The ceiling camera and lamp, along with the two first-surface mirrors that formed a periscope, were supported in the light-fixture housing by an aluminum structure (Fig. 7). The structure slid into the housing from above and was

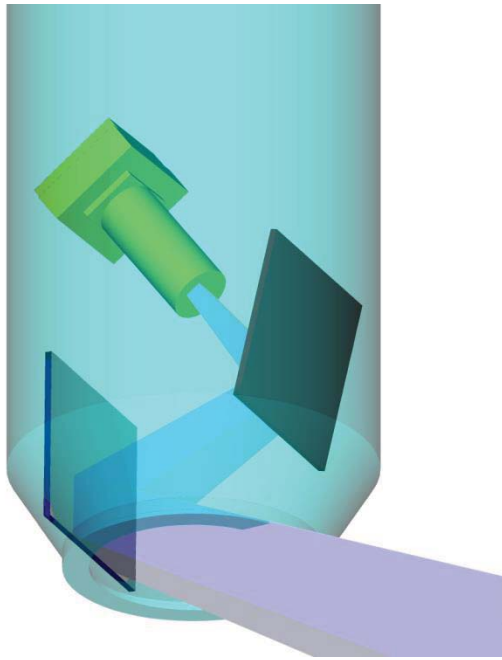


Figure 6. Schematic showing folded light path of camera mounted in ceiling light-fixture housing.

clamped to a flange at the top of the housing. A 0.25-in thick window at the bottom of the structure replaced the lens of the light fixture. The pitch angles of the camera and lamp (mounted together) and the two mirrors (mounted separately) were independently adjustable from above to allow alignment fine-tuning after the periscope was installed. The azimuth point angle was adjusted by rotating the structure as a unit about its vertical axis within the lamp housing. Vacuum grease was applied to a seal at the bottom of the housing to facilitate this adjustment. The lens was focused before installation at the distance to the background. There was no provision for adjusting focus or aperture of the lens from above. Power supplies and controllers for the camera and lamp were mounted outside of the lamp housing.

Both cameras were connected to the data-acquisition computer, which was located on a nearby cat-walk, by fiber optic cables. The data-acquisition computer was operated remotely from the control room via a KVM switch. Both lamps and cameras were triggered by a once-per-revolution signal from the rotor provided by a Rotor Azimuth Synchronization Program (RASP) USB box (Ref. 33) that allowed measurements to be acquired at different azimuth angles of the rotor. The camera integration time and duration of the lamp flashes were both 40 μ s. In this time interval, the rotor tip, traveling at 718 ft/sec (258 RPM), would advance only about 0.0287 ft (0.34 in) or 0.016 chord lengths. At the magnification of the cameras, this corresponded to about 14 pixels.



Figure 7. Photograph of structure that supported ceiling-mounted camera and mirrors before it was installed in the light fixture housing.

Retro-Reflective Background

Eight contiguous 4- by 4-ft acoustic panels nearly filled the backgrounds of both cameras. Because the sidewalls were actually polygonal rather than circular, the acoustic panels were not segments of a circle. Rather, each panel was creased down the middle to form two flat halves with an angle difference of 11.25°. Quarter-inch aluminum plating was cut to fit the shape of these panels. The plates were covered with retro-reflective material (Scotchlite™ Very High Gain Sheeting 3000X, Ref. 34), splattered with black ink, and mounted over the appropriate acoustic panels. The retro-reflective panels are visible in Figures 3 and 8.

Camera Calibration Structure

The cameras were calibrated in situ by imaging a calibration structure that was placed in the region of interest. This structure included 65 targets that were well-distributed within the ROI and whose relative spatial coordinates were known. The structure was built from ABS pipe and was supported approximately 20 feet above the floor of the test section by an aluminum mast that was stabilized by guy wires. The guy wires were adjusted until the mast was vertical as indicated by a laser level. The structure itself consisted of a 9-ft long, 3-in diameter horizontal pipe that was oriented in the span-wise direction (Figure 8). Spokes extended radially outward from this crossbar at regular span-wise intervals. One-quarter-inch diameter retro-reflective targets were glued at 6-inch intervals to the sides of the spokes nearest the cameras. Plumb bobs were suspended from the ends of the cross bar and their positions were marked on the tunnel floor. Virtual imaging was used to design the structure and verify that the targets were viewable by both cameras, were well-distributed within the fields of view, and were the proper size for locating with target-finding software. Once the structure was in place, it was

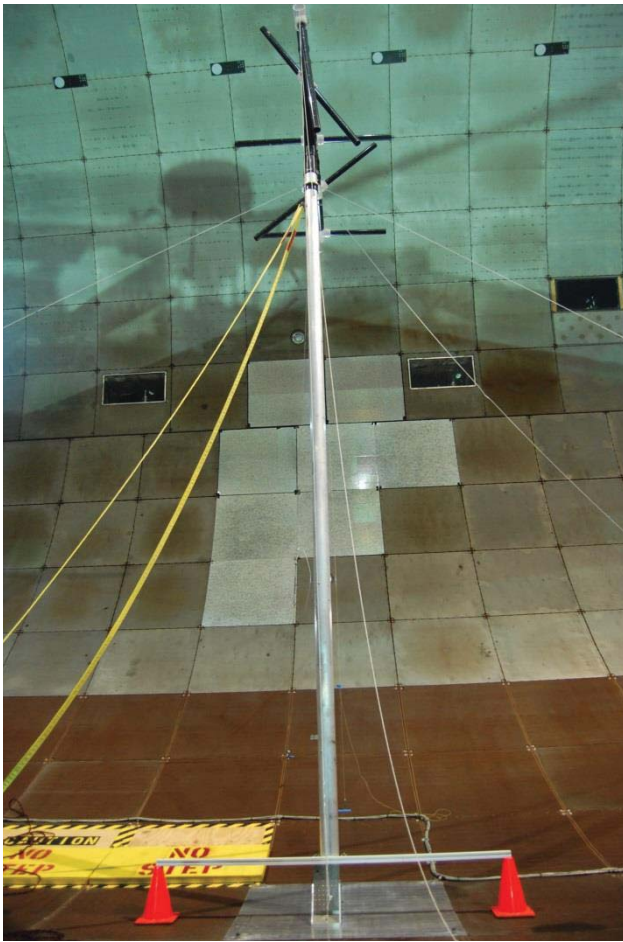


Figure 8. Structure used to calibrate the cameras. Eight retro-reflective panels are in the background.

imaged with both cameras with illumination provided by the LED flash lamps.

DATA ACQUISITION

Data images were acquired semi-manually once the tunnel and rotor were at the desired test condition. The desired azimuthal angle was input in the RASP control software, and data acquisition was initiated by clicking a record button in the camera-control software. The software began acquiring images from both cameras, one per revolution as triggered by the RASP. For most cases the dwell time at the test condition was long enough to allow acquisition of 20–30 RBOS images at more than one azimuth delay—2 or 3 azimuth delay points were typical. For test points where the dwell time was very long (e.g., points where blade-displacement measurements were made), RBOS images were often acquired at 5° intervals over a range of azimuth angles between 0–90°. Images acquired at the same test condition but at different azimuth angles were not acquired during the same pass of the rotor blade.

To avoid interference with PIV data acquisition, RBOS images were not acquired during the PIV runs. Instead, they were acquired during separate runs where the test conditions

were the same as for the PIV measurements. In addition to the PIV test conditions, RBOS images were acquired at almost every other test condition as well—more than 2000 in all. The total volume of RBOS image data was about 208,350 images, which required 3.04 TB of storage.

Reference Wind-Off Images

“Same-day” reference images were taken at the beginning and end of each shift, with the flow in the tunnel at zero velocity. Ideally, the speckle-displacement distribution of each of these reference images relative to another would be uniformly zero, indicating no density variations. However, throughout the test it was discovered that speckle displacements between two ostensibly identical wind-off images were as large as those due to vortices measured at wind-on conditions. In addition, the distributions varied randomly from one reference image to the next. The source of this problem was traced to heat generated by the LRTA and instrumentation hat, which lay directly below the line-of-sight of the sidewall camera. All attempts to acquire wind-off images without this heat contamination, which included turning off all known heat sources to the test article overnight and even over weekends, failed until, finally, satisfactory reference images were acquired after the LRTA was removed from the test section at the end of the test. The ceiling camera was less affected by the heat convection because the line-of-sight to the ROI was not as close to the hub. The improvement in the post-test reference images from the ceiling camera was offset by the fact that the camera had been jostled by repeated opening and closing of the ceiling clam-shell doors. The best results were obtained using same-day reference images for the ceiling camera and post-test reference images for the sidewall camera.

DATA REDUCTION

Data reduction involved the following steps:

1. *Calibrate the cameras using images of the calibration structure.*

Targets on the calibration structure were identified in the calibration image of each camera, and the DLT was computed from Equation 3 using the assumed spatial coordinates of the targets. The space coordinates were then adjusted to minimize the RMS re-projection error, and the DLTs of both cameras were recomputed at each step.

The Fundamental matrix was also computed from the image coordinates of the calibration targets in the images of both cameras. The space coordinates of the targets do not enter into this calculation.

2. *Compute speckle-displacement distributions.*

Speckle displacements were determined by comparing each wind-on image to a reference wind-off image. A dense rectangular grid was

defined that overlay the images. Speckle displacements were computed at each node by defining a small interrogation window (20 x 20 pixels) and extracting image-intensity data from both the wind-on and wind-off images within that window. The density of the grid was defined so that there was 50% overlap between adjacent interrogation windows. The intensity data were then cross correlated resulting in a two-dimensional correlation function that included a sharp peak if there was correlation between the images within the window. The offset of this peak in each direction from the center of the window was equal to the offset of the two images relative to each other. This procedure results in a distribution of displacements that, if represented by grey-level contours proportional to the displacement, appears much like a schlieren image. Displacements in arbitrary directions may be computed and displayed. This is equivalent to rotating a knife edge of a schlieren system to highlight density gradients in different directions.

Most of the wind-on images exhibited a small global shift in the speckled background that was due to very slight contraction of the test section as the static pressure inside decreased below ambient pressure outside. To account for this shift, the speckle displacement at a reference point in the quiescent flow was measured by cross-correlating the wind-on and wind-off images in a large (256 x 256 pixel) interrogation window centered on the reference point. This offset was then subtracted from the speckle displacements measured at each data point. This procedure also corrected for small wind-on camera shifts due to vibration.

3. *Identify vortex filaments in the speckle-displacement data.*

The position of each vortex in each image was approximated by a series of points that overlay the filament in the speckle-displacement data. Several algorithms were developed to automatically find the vortices, but these were reliable only in low-noise data. For most cases the vortices were identified by pointing and clicking on a display of the speckle-displacement distribution. Locating vortices in the data was made more difficult by the presence of lines in the data due to the creases in the acoustic panels and seams between sheets of retro-reflective material in the background. There was usually noticeable cycle-to-cycle variation in the positions of the vortices. Therefore, averaging data over many cycles as a way to improve the signal-to-noise was not appropriate since the vortices would be smeared. Thus all of the

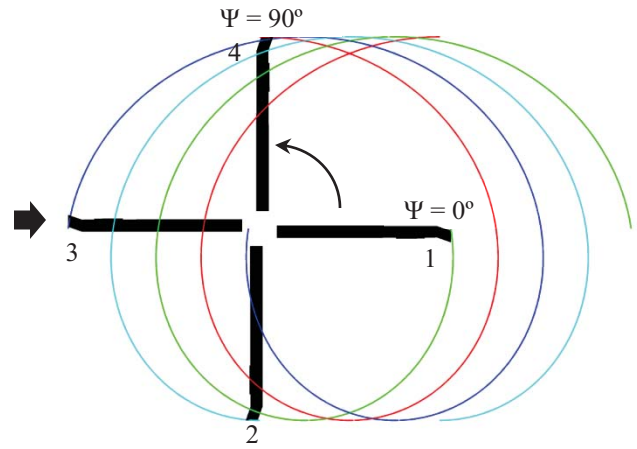


Figure 9. Vortex convection model used to guide pairing of vortices. Flow is from left, advancing blade is at top ($\mu = 0.15$).

measurements are instantaneous based on data from a single image from each camera.

4. *Pair vortices between the two cameras.*

Next, vortices in each image were paired between the two cameras. Identifying which vortex was from the tip of the most recent blade passage was usually obvious, especially for small azimuth delays where the tip was in the fields of view. But for many cases, some where up to 10 vortices were visible, pairing was much more difficult. The clarity of a vortex in the data and/or a distinctive shape sometimes was used as matching criteria. In some difficult cases, pairing could be established by observing a sequence of parametric data and tracing the evolution of the vortices back to a condition where the pairing was clear. Every potential vortex pairing corresponded to a line in space that was consistent with the lines-of-sight of both cameras, but incorrect pairings resulted in vortex positions that did not make physical sense. Pairings were chosen that yielded vortices with positions in the x - y plane that were consistent with a simple vortex-convection model. By this model, vortices from previous blade passages lie progressively further inboard as they pass through the ROI, as shown in in Figure 9.

5. *Establish camera A to B correspondence of points along each vortex filament.*

Correspondence for each point on the vortex in camera A was established by computing the corresponding epipolar line in camera B data. The corresponding point in camera B was the intersection of the vortex in camera B and this epipolar line. For example, in Figure 10 the cyan line in image B is the epipolar line corresponding to the cyan dot in image A.

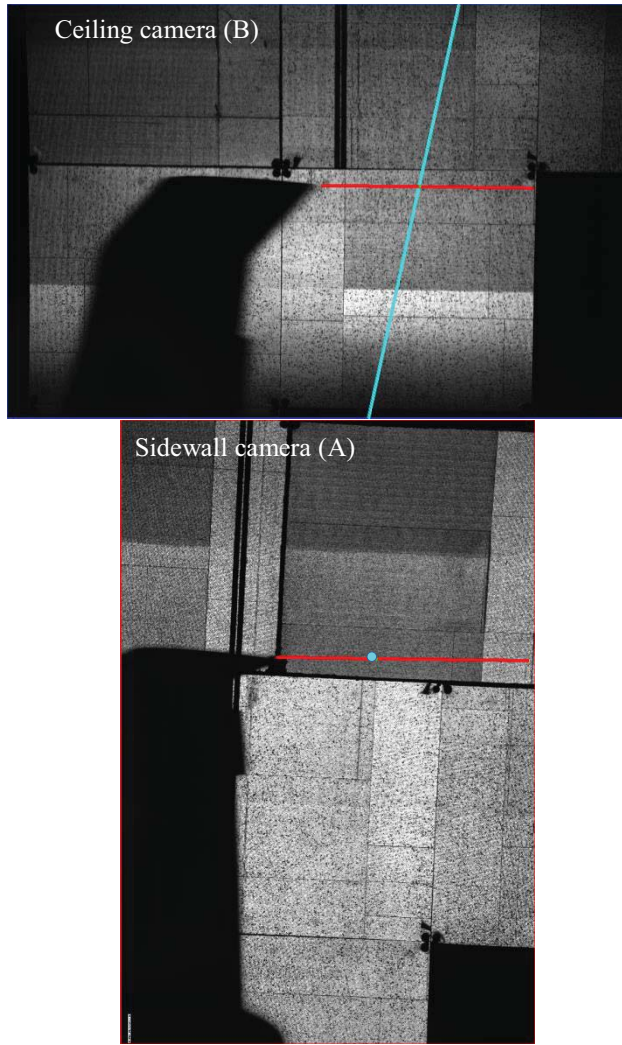


Figure 10. Raw images from ceiling (B, top) and sidewall (A, bottom) cameras that show how epipolar lines were used to establish corresponding points on a vortex (red line). Rotor tip moves from right to left, flow is left to right. The cyan epipolar line in the top image (camera B) corresponds to the cyan point on the vortex in the lower image (camera A).

6. *Compute object-space coordinates.*

Equation 4 was used to compute the space coordinates of each pair of corresponding points in images from cameras *A* and *B*.

7. *Compute where and at what angles the vortex filaments pass through the PIV plane.*

The x - y and x - z coordinates of each vortex filament were curve-fit using cubic splines with some smoothing, and the point of intersection of the splines with the PIV plane was determined knowing the x coordinate of the plane. The local angles of the filament in the x - y (θ) and x - z (ϕ) planes at the point of intersection were computed from the

coordinates of the two sequential filament points that lay on opposite sides of the PIV plane.

All data reduction was performed using custom software that was developed in house.

RESULTS

The UH-60A Airloads test included many parametric test points where test conditions were systematically altered, one variable at a time. The parametric variables included advance ratio (μ), normalized thrust coefficient (C_T/σ), rotor shaft angle (α), and tip Mach number (M_{tip}). This section presents RBOS vortex-position measurements from a sequence of parametric test points that included the test conditions where PIV data were later acquired. The effects on vortex positions of advance ratio (μ), normalized thrust coefficient (C_T/σ), and blade azimuth angle (ψ) are illustrated. Finally, RBOS images are shown for a variety of test conditions that include interesting flow features in addition to vortices.

In this paper, each tip vortex in the ROI shall be referred to by the rotor blade that produced it. The order of blade passage through the ROI is 1-2-3-4-1 etc. The corresponding order of vortices in the ROI by increasing age is 1-4-3-2-1 etc. Thus, when ordered by age, the vortex sequence is the inverse of the blade-passages order.

Vortex pairings and their interpretations would be very difficult to ascertain if the data were considered in isolation. They are based on a comprehensive examination of data from many test conditions. As will be shown, these pairings result in vortex positions that are consistent with PIV measurements and with the simple vortex convection model.

Case 1: $\alpha = 0^\circ$, $\mu = 0.15$, $C_T/\sigma = 0.12$ (Run 42 pt 18)

Figure 11 shows instantaneous speckle-displacement distributions measured by the sidewall and ceiling cameras at three rotor azimuth angles ($\psi = 5^\circ$, 7° , and 15°) where $\alpha = 0^\circ$, $\mu = 0.15$, and $C_T/\sigma = 0.12$. This was a relatively high thrust, low advance-ratio case where the visibility of vortices in the RBOS data was particularly good. At the rotor azimuth angles shown, rotor blade 4 had just passed through the laser plane and was moving upstream (from right to left in the image). The outboard portion of the blade, including the swept tip and trim tab, appears in the data from both cameras as randomly speckled regions with uncorrelated data. The lower-right corner in both views also includes a rectangular region of uncorrelated data that corresponds to a background panel that was not covered with retro-reflective material. The two vertical stripes beyond the blade tip are lines on the background that were used to assist alignment of the PIV laser sheets. Other vertical and horizontal lines are joints between retro-reflective panels and creases in the panels.

Multiple vortices are visible in the data from both cameras. Most clearly shown in both views is the vortex (4) that extends downstream from the trailing edge of the swept

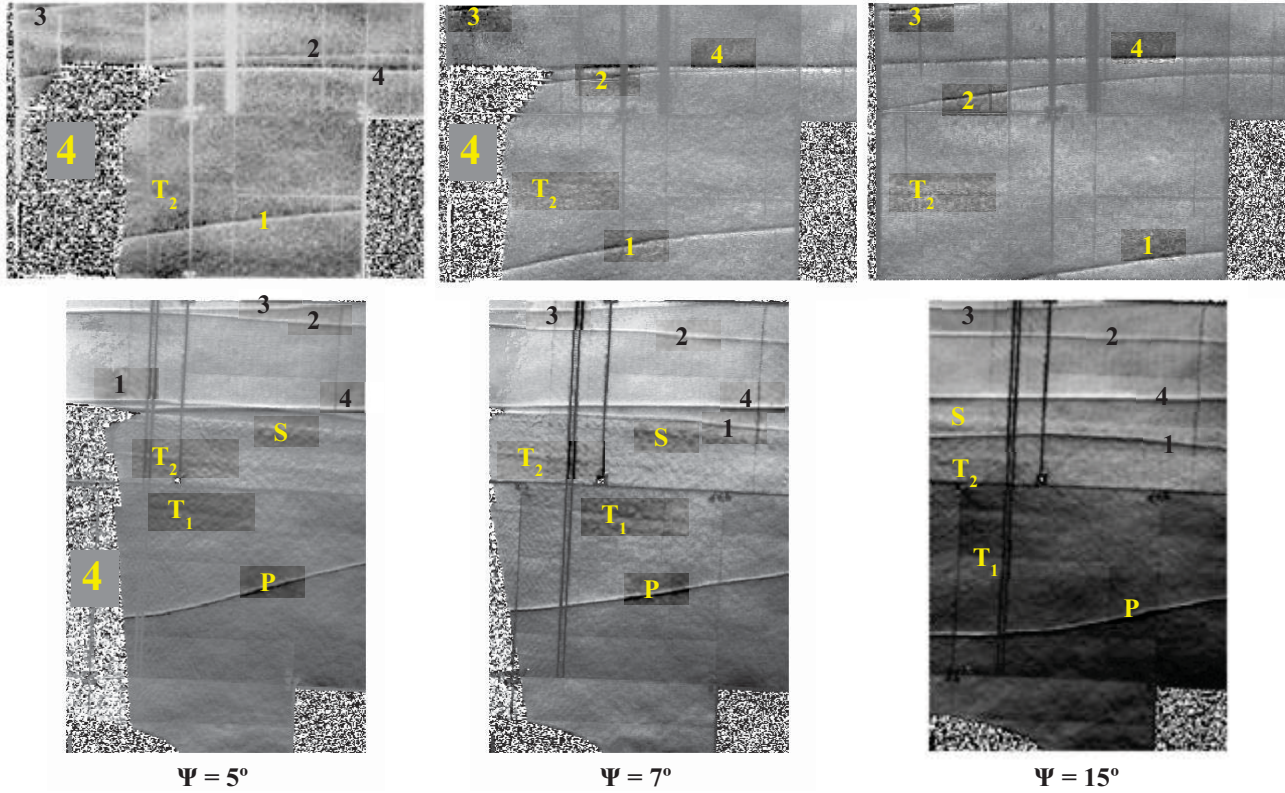


Figure 11. Speckle-displacement distributions for ceiling (top) and sidewall (bottom) cameras at three azimuth angles. Blade 4 is in the ROI (Case 1: $\alpha = 0^\circ$, $\mu = 0.15$, $C_T / \sigma = 0.12$).

tip. Clearly this is the youngest vortex and was generated by blade 4 during its current pass through the ROI. There is little change in the position of this vortex as the azimuth angle increases. The origins and pairings of the other vortices are much less obvious. The next youngest vortex, produced by blade 3, which had just passed over the nose of the LRTA, appears at the very top of both images. Only a small segment of this vortex is visible in the upper-left corner of the data from the ceiling camera and the position changes very little with ψ . The vortex from blade 2, in retreat on the port side of the LRTA, is just below vortex 3 in the sidewall view and, at $\psi = 5^\circ$, just above vortex 4 in the ceiling view. This vortex is displaced downward in both views as ψ increases. Finally, the vortex from blade 1, which had just passed over the aft end of the LRTA, is almost coincident with vortex 4 in the sidewall view at $\psi = 5^\circ$, and is well below all other vortices in the ceiling view. The blade-1 vortex is displaced downward in both views as ψ increases. A prominent vortex (P) in the sidewall views has no pair in the ceiling view. The lateral extents, or diameters, of all of the vortex filaments are about the same—they do not appear to increase with vortex age.

The speckle-displacement distributions reveal other flow features of interest. In the sidewall view there is a disturbance (S) just below vortex 4 that also propagates downstream from the rotor tip. This disturbance is not nearly as well defined as the tip vortices and appears to expand and

become more diffuse with both distance downstream and increasing ψ . By $\psi = 15^\circ$ the disturbance is barely detectable. In the ceiling view there is only the slightest hint of this feature at $\psi = 5^\circ$, and it is not visible at all at larger ψ .

The sidewall views at $\psi = 5^\circ$ and $\psi = 7^\circ$ also reveal similar disturbances that propagate downstream from the outboard (T_2) and inboard (T_1) edges of the trim tab. By $\psi = 15^\circ$ these disturbances have nearly disappeared. In views from the ceiling camera, the outboard disturbance (T_2) is barely visible, and the inboard disturbance is beyond the field of view. Finally, in the sidewall view, the magnitude of background disturbances appears to be less outboard of the rotor tip than inboard, indicating relatively quiescent flow. This difference is less apparent in the ceiling view because of the lower SNR.

The object-space coordinates of points on each vortex filament were determined as described in the Data Reduction section. Figure 12 shows views of these vortices from x , y , and z directions. The rotor is also shown for reference; its position, however, is based only on ψ , not on measurements, and does not account for rotor lag, flapping, or angle of attack. Also shown for reference is the PIV measurement region. The data at each ψ are instantaneous. Only vortices 4, 2, and 1 are shown. Vortex 3, the second youngest vortex after 4, was barely visible in the ceiling view, and none of the points that did appear were common to those in the sidewall view. Note in the x and z views that the vortices

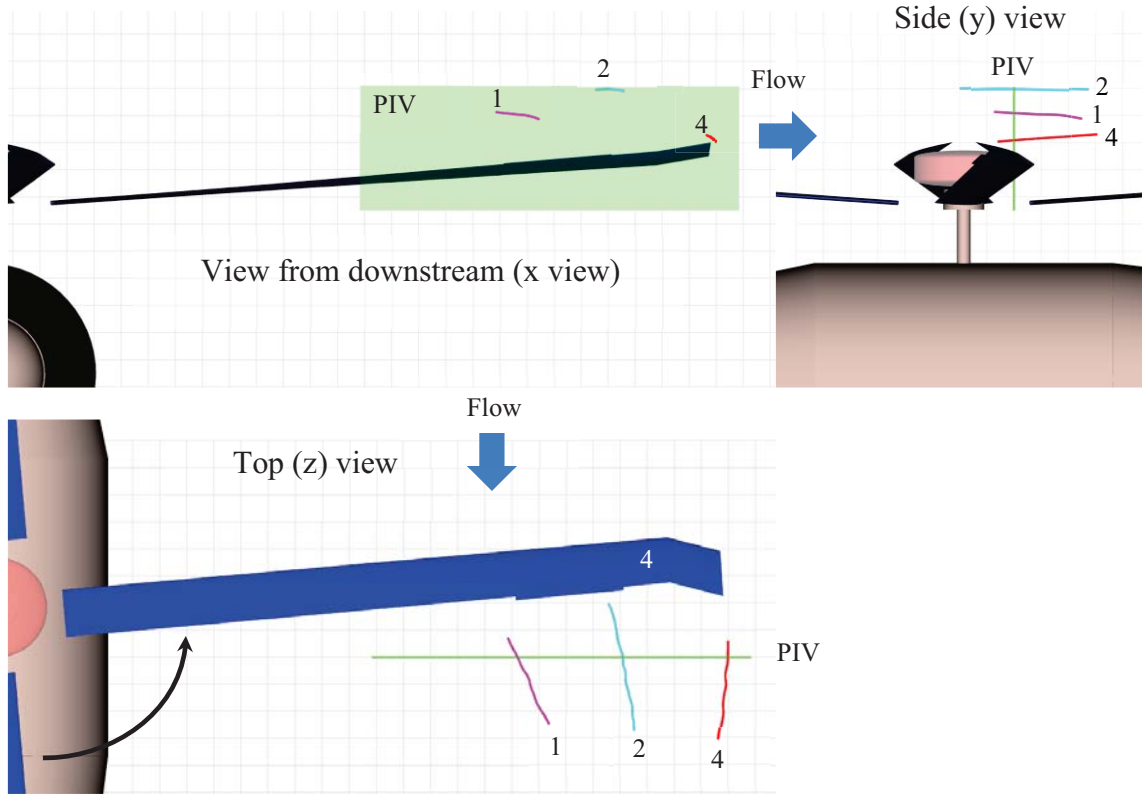


Figure 12. Schematic views showing vortices at $\psi = 5^\circ$ (Case 1: $\alpha = 0^\circ$, $\mu = 0.15$, $C_T / \sigma = 0.12$).

move inboard as they age, as required by the vortex-convection model. This result is not surprising since the convection model was used to guide the pairing of vortices. The convection model, however, says nothing about the vertical displacement of the vortices. This is shown in the x and z views. The vortices initially move upward as they age and move inboard. Vortex 2 is near the upper edge of the PIV region. Vortex 3 is not shown but, because it appeared high in the views of both cameras, it would likely lie above the PIV measurement region and at a span station between vortices 4 and 2. The oldest vortex (1) lies above the youngest (4) but below the next oldest (2).

The view from above (z) shows that the two older vortices (1) and (2) are yawed inboard whereas the youngest vortex (4) is yawed slightly outboard. The inboard yaw of the older vortices is expected by the convection model (Fig. 9). The y -view shows that the youngest vortex (4) is pitched down slightly whereas the oldest vortex (1) is pitched up. The pitch angle of vortex 2 is nearly zero. These trends remain unchanged over $\psi = 5^\circ$ – 15° .

Case 2: $\alpha = 0^\circ$, $\mu = 0.15$, $C_T / \sigma = 0.08$ (Run 42 pts 11-12)

For this case, the test conditions were the same as when PIV data were later acquired (Run 73). The visibility of the vortices was not as good as for Case 1 because of the lower thrust. This was especially true for the ceiling view, where

the SNR was lower than for the sidewall view. Nonetheless, at $\psi = 90^\circ$, when the tip trailing edge of blade 1 was in the PIV plane, vortices from the three most recent blade passages (1, 4, and 3) were discerned in the speckle-displacement distributions from both cameras (Figure 13). The disturbance (S) from the tip is more pronounced in the sidewall view than in Case 1. There is a disturbance in the ceiling view about halfway outboard on the swept tip (S ?) that may be the same feature. Disturbances from the outboard edge of the trim tab (T_2) are clear in both views. Note that the numbering of the vortices has been incremented by 1 compared to Case 1 because at $\psi = 90^\circ$ blade 1 rather than blade 4 was in the ROI. Thus, in order of increasing age, the vortices were 1, 4, 3, 2 (not visible).

RBOS data were acquired at more than 100 consecutive rotor revolutions at this condition. At each revolution the position of the blade-tip trailing edge was computed since it was visible in the images from both cameras. Figure 14 shows the positions of the three youngest tip vortices as they passed through the PIV plane. The positions are relative to the instantaneous position of the tip trailing edge. Data for all revolutions are shown as well as the average positions. The youngest vortex (1) is slightly outboard of the rotor tip, but at the same height. The data from multiple revolutions are not randomly distributed about a mean position and show what might be a slight bias due to small systematic errors in locating corresponding points on the vortex filament. The

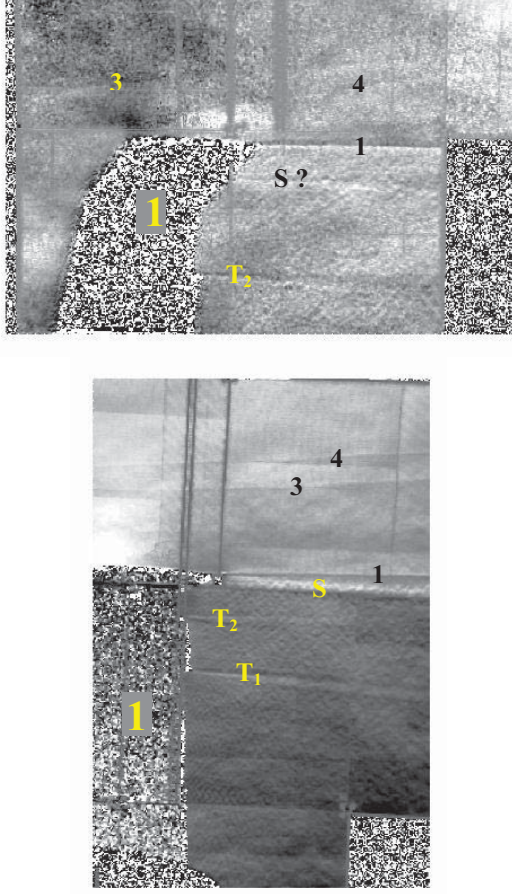


Figure 13. Speckle-displacement data from ceiling (top) and sidewall (bottom) cameras. Blade 1 is in the ROI. (Case 2: $\alpha = 0^\circ$, $\mu = 0.15$, $C_T / \sigma = 0.08$, $\psi = 90^\circ$).

next older vortex (4) lies above and inboard of the rotor tip, and the measurements from multiple revolutions are more randomly distributed about the mean position. Likewise, the next older vortex (3) lies further inboard and above both of the younger vortices.

Figure 15 is a y - z plot at the same condition but in a plane 30 inches (0.09 rotor radii) downstream of the PIV plane. In this plane the youngest vortex (1) is slightly higher and further inboard than its position in the PIV plane. The two older vortices (4 and 3) are also slightly higher but further outboard.

Figure 16 shows data in the PIV plane at the same test conditions but for $\psi = 75^\circ$. At this azimuth only two vortices were visible in the speckle-displacement data: the youngest vortex (from blade 4), and the next older (from blade 3). Data are shown for 20 rotor revolutions relative to the rotor tip position measured at $\psi = 90^\circ$ —the same reference as for Figs. 14 and 15. At this azimuth, the youngest vortex (blade 4) has moved higher and slightly inboard compared to

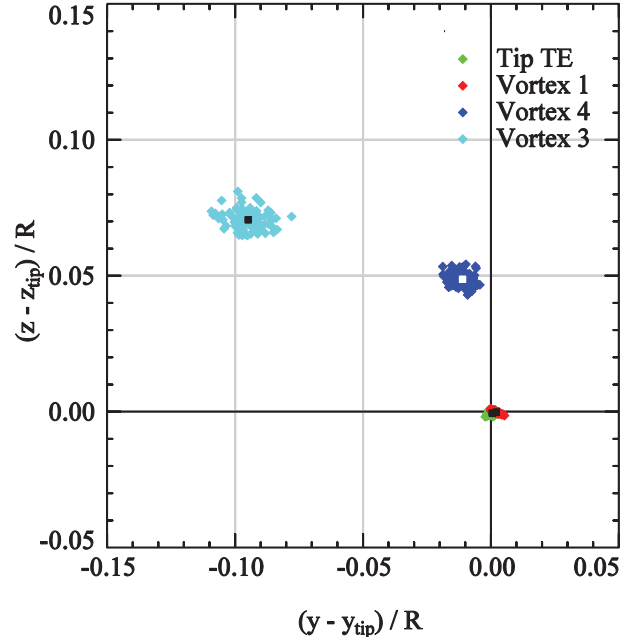


Figure 14. Instantaneous vortex positions in PIV plane relative to instantaneous blade-tip trailing edge. Average value is shown in center of each distribution. (Case 2: $\alpha = 0^\circ$, $\mu = 0.15$, $C_T / \sigma = 0.08$, $\psi = 90^\circ$).

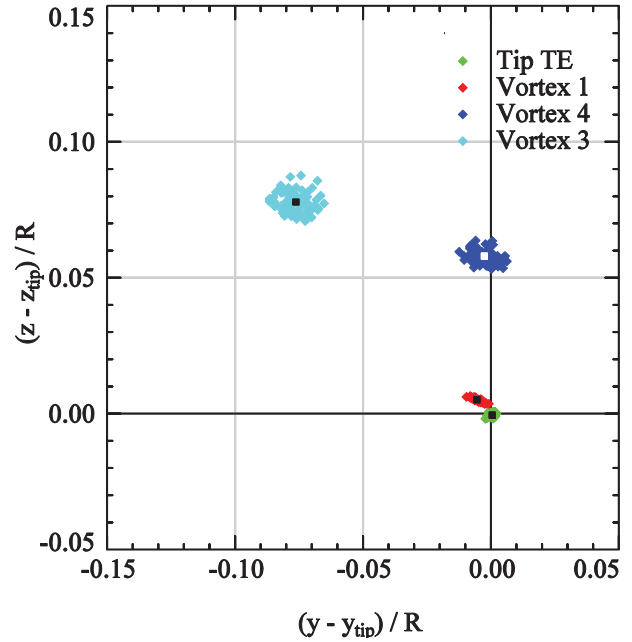


Figure 15. Instantaneous vortex positions 0.09 rotor radii downstream of PIV plane relative to instantaneous blade-tip trailing edge. Average value is shown in center of each distribution. (Case 2: $\alpha = 0^\circ$, $\mu = 0.15$, $C_T / \sigma = 0.08$, $\psi = 90^\circ$).

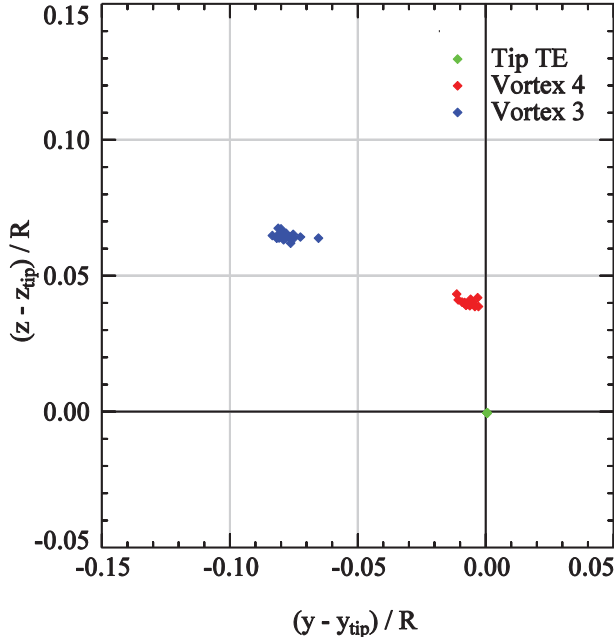


Figure 16. Instantaneous vortex positions in PIV plane relative to instantaneous blade-tip trailing edge (Case 2: $\alpha = 0^\circ$, $\mu = 0.15$, $C_T / \sigma = 0.08$, $\psi = 75^\circ$).

$\Psi = 90^\circ$, and the next older vortex (blade 3) has moved inboard and up. After another 15° of rotation, when blade 1 passes through the ROI, the blade 4 and 3 vortices become the second and third youngest vortices, respectively. Note that both vortices in Figure 16 are approaching the positions of the second and third youngest vortices in Figure 14.

Effects of Thrust Coefficient and Advance Ratio on Vortex Positions (Run 42)

The effects of C_T / σ on the positions of vortices passing through the PIV plane are shown in Figure 17. Twenty revolutions of data at four thrust coefficients are shown. Azimuth angle (ψ) is 5° , $\alpha = 0^\circ$, and $\mu = 0.15$ (same as for cases 1 and 2). Four vortices, one from each blade, are shown at $C_T / \sigma = 0.10$. The two youngest vortices (4 and 3) are shown at $C_T / \sigma = 0.08$, and vortices 4 and 2 are shown at the two highest thrust levels (vortex 3, the second youngest, was presumably too high to be seen). All of the measurements are relative to the tip position of blade 1 at $\psi = 90^\circ$ and $C_T / \sigma = 0.08$ (same reference as for case 2). Therefore, these data show absolute positions of the vortices, not positions relative to the rotor tip at each condition, which also changes with thrust coefficient.

Figure 18 shows the effects of changing advance ratio on vortex positions in the PIV plane ($C_T / \sigma = 0.12$, $\alpha = 0^\circ$, $\psi = 5^\circ$). Vortex measurements for 20 rotor revolutions are shown at three advance ratios: $\mu = 0.15$, 0.20, and 0.24. The same blade tip reference is used as in Figure 16. The youngest and two oldest vortices are shown for $\mu = 0.15$ (same data as Case 1); the three youngest vortices are shown

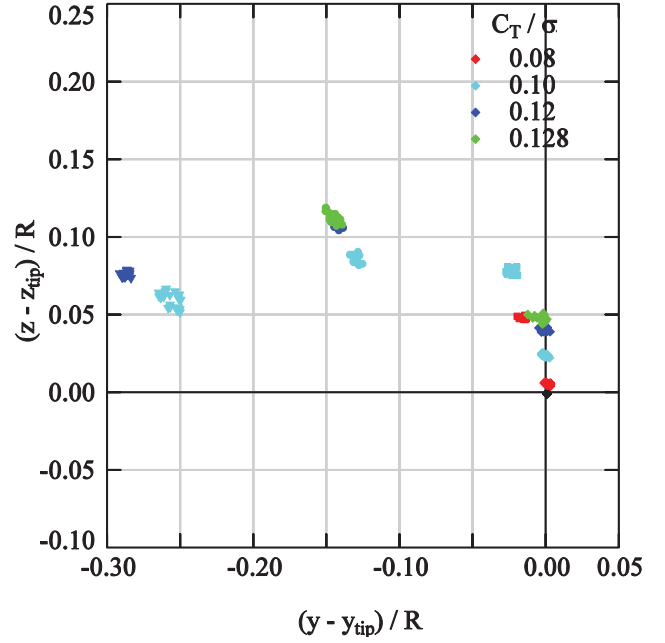


Figure 17. Effect of thrust coefficient on vortex positions in PIV plane ($\alpha = 0^\circ$, $\mu = 0.15$, $\psi = 5^\circ$).

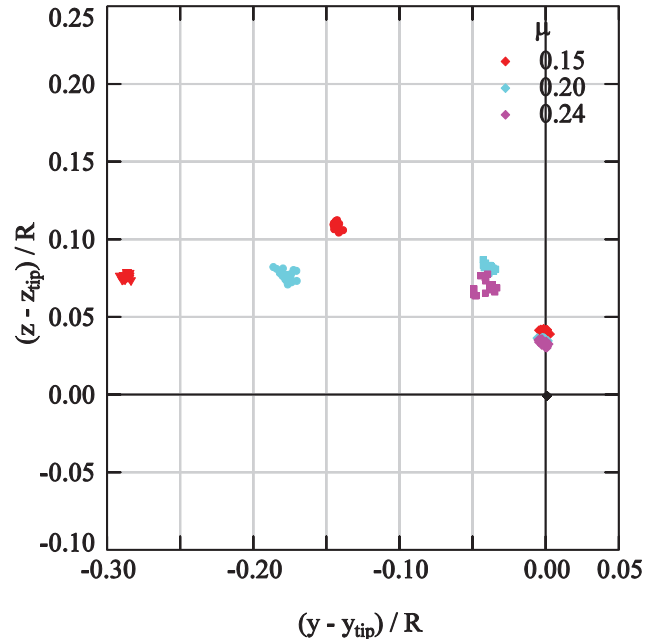


Figure 18. Effect of advance ratio on vortex positions in PIV plane ($\alpha = 0^\circ$, $C_T / \sigma = 0.12$, $\psi = 5^\circ$).

for $\mu = 0.20$ (Run 42 Pt 30); and the two youngest are shown at $\mu = 0.24$ (Run 42 Pt 45).

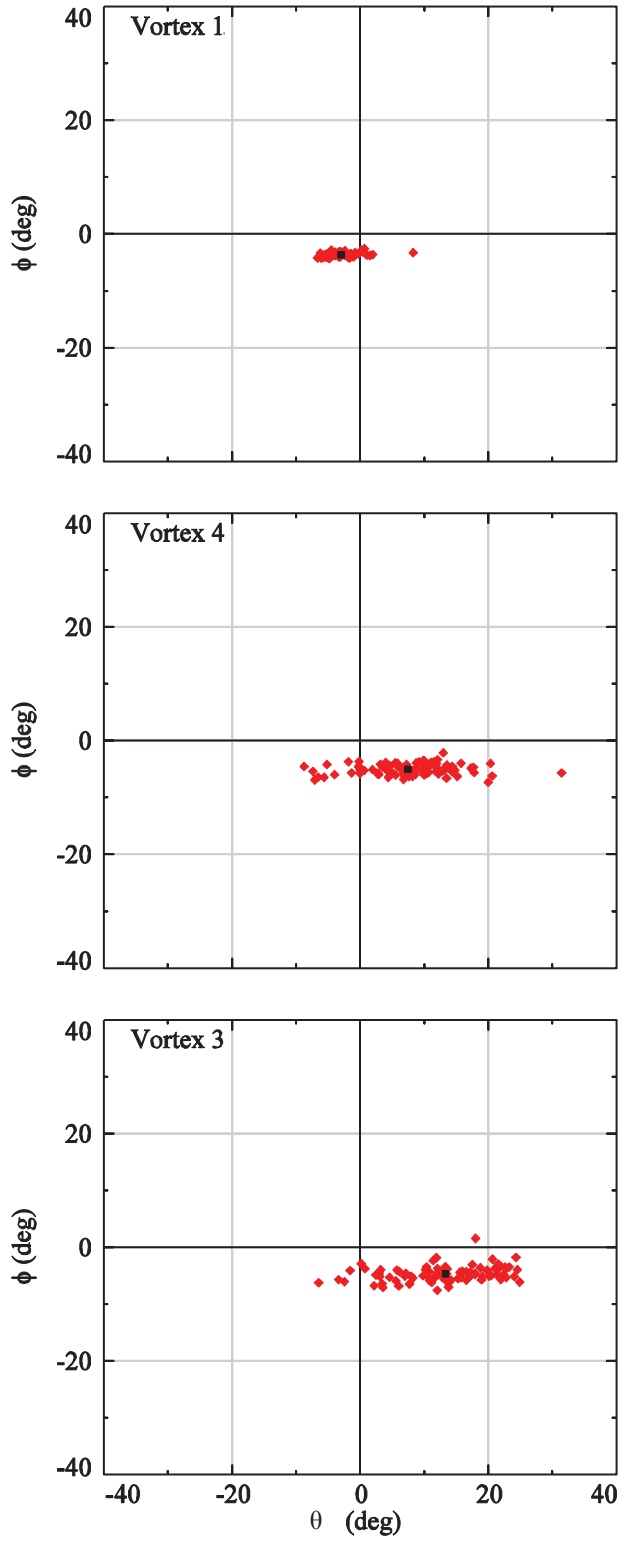


Figure 19. Instantaneous vortex angles at PIV plane. Average values are shown as black squares (Case 2: $\alpha = 0^\circ$, $\mu = 0.15$, $C_T / \sigma = 0.08$, $\psi = 90^\circ$).

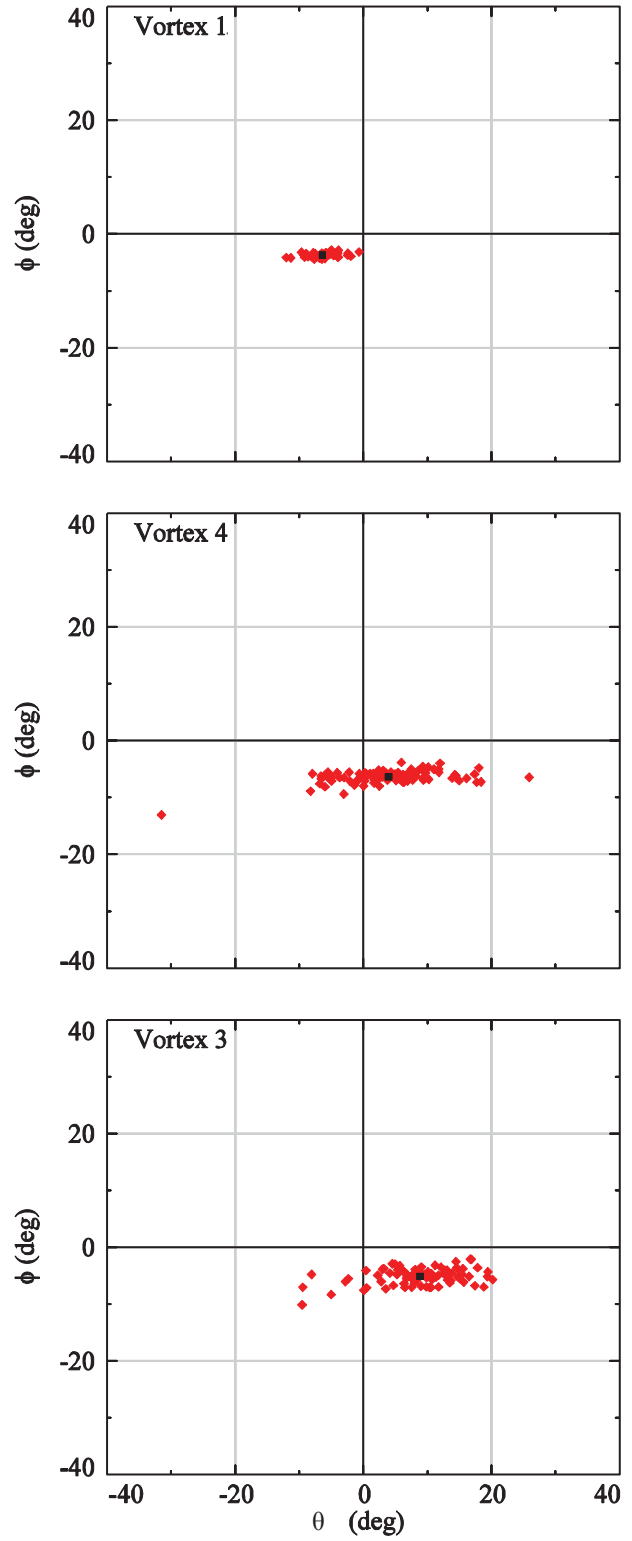


Figure 20. Instantaneous vortex angles 0.09 rotor radii downstream of PIV plane. Average values are shown as black squares (Case 2: $\alpha = 0^\circ$, $\mu = 0.15$, $C_T / \sigma = 0.08$, $\psi = 90^\circ$).

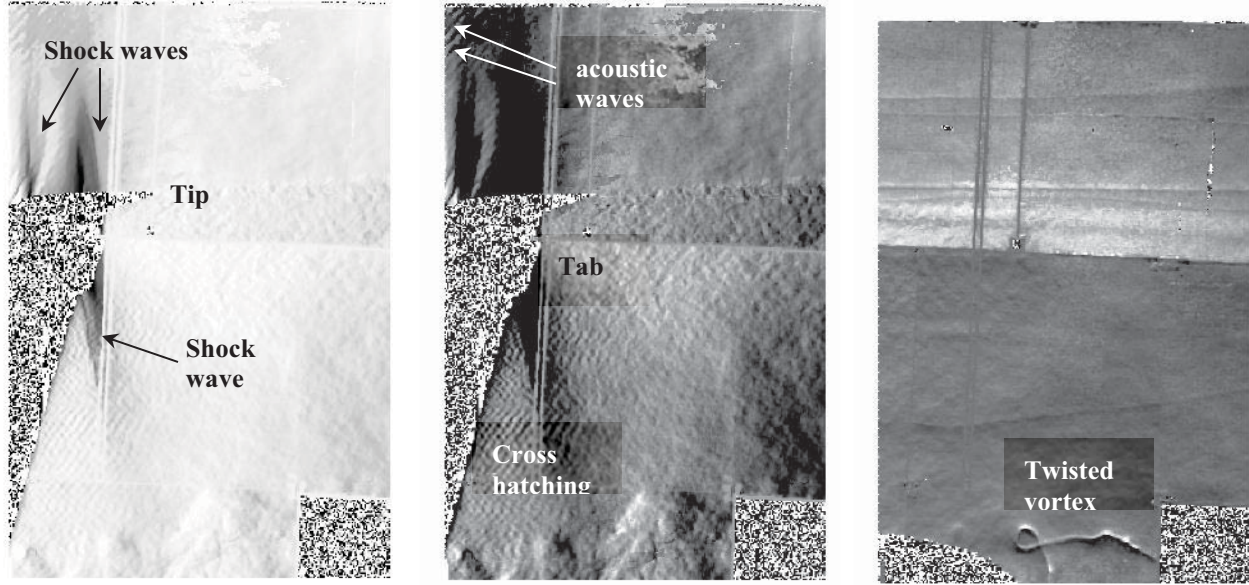


Figure 21. RBOS flow visualizations. The data at left and center are from the same image ($\alpha = -8^\circ$, $\mu = 0.35$, $C_T / \sigma = 0.1$, $M_{\text{Tip}} = 0.675$, $\psi = 5^\circ$). The virtual knife edge is vertical at left and highlights shock waves on the blade tip. The knife edge is 45° in the center to highlight acoustic waves and cross hatching. The data at right are from a different run ($\alpha = 0^\circ$, $\mu = 0.10$, $C_T / \sigma = 0.1$, $\psi = 15^\circ$) and reveals a twisted vortex.

Vortex Angles

Figure 19 shows the instantaneous angles of the vortex filaments at the PIV plane for $\psi = 90^\circ$ (Case 2). The angle in the vertical x - z plane (ϕ) is plotted versus the angle in the horizontal x - y plane (θ) for each vortex. Average values are indicated by the black symbols. Figure 20 shows data for the same vortices but at a parallel plane 0.09 rotor radii further downstream. The youngest vortex (1) is inclined slightly outboard (negative θ) at both planes, whereas the two older vortices (4 and 3) are inclined inboard. The angle increases with vortex age (compare vortices 4 and 3) but decreases with distance downstream (compare Figures 19 and 20). All three vortices are inclined downward at both planes, and there is little change in the vertical angle with either vortex age or distance downstream. The dispersion of the instantaneous angle measurements is much greater in the horizontal plane than in the vertical plane.

Interesting Flow Features Visualized by RBOS

The RBOS speckle-displacement data revealed interesting flow features in addition to vortices. Shock waves on both the upper and lower surfaces of the rotor tip were clear in data from the sidewall camera for cases where the Mach number of the advancing blade relative to the oncoming flow was high. In Figure 21 (left), two shock waves are visible on the upper surface and at least one is visible on the lower surface for a case where the resultant tip Mach number was about 0.91 (RPM = 268, $\mu = 0.35$, $\psi = 5^\circ$, $C_T / \sigma = 0.1$). Speckle displacements are shown in the streamwise direction, and the limits of the grayscale were adjusted to

improve visibility of the shock waves. Figure 21 (center) shows the same data but with the virtual knife edge rotated 45° . The grayscale was set to highlight cross-hatching immediately downstream of the trailing edge inboard of the tab and spherical acoustic waves emanating from the rotor tip. Figure 21 (right) was acquired at a different condition ($\alpha = 0^\circ$, $\mu = 0.10$, $C_T / \sigma = 0.1$, $\psi = 15^\circ$) and shows a twisted vortex. This vortex was beyond the field of view of the ceiling camera, so no space coordinates were computed.

DISCUSSION

The RBOS/photogrammetry measurements from Case 2 (Run 42 Point 11) have been compared to PIV measurements (Ref. 35) acquired during a different run at the same test conditions (Run 73). The locations where the vortex filaments passed through the PIV plane were found to be in good agreement with the positions determined from the PIV data. Both measurements showed the same trajectory of vortices in this plane: vortices initially move inboard and upward as they age, then the upward displacement decreases but the inboard displacement continues. When projected into the x - y plane, this behavior is consistent with the simple vortex convection model.

In addition to the vortices from the blade tips, the PIV measurements show a region of distributed vorticity between the outboard edge of the trim tab and the rotor tip. This region is initially at the same height as the blade and is much wider (spanwise, y) than it is high (vertical, z). The vorticity,

however, “rolls up” and moves upward, becoming a more distinct cylindrical vortex with vorticity of the same sign as the tip vortices. Whether this vortex appears in the RBOS data is unclear. The vortex may correspond to the disturbance “S” that appears to propagate from the rotor tip in data from the sidewall camera and is very faint in the data from the ceiling camera (Figure 13). At young wake ages, when the disturbance is much wider than it is high, the optical path through the disturbance along the line-of-sight to the sidewall camera is much longer than for the ceiling camera. Therefore, larger speckle displacements and higher visibility would be expected. However, after the vortex rolls up and becomes cylindrical, this difference should disappear. The feature that appears in the data from the ceiling camera at young wake ages quickly becomes lost in the background noise at older ages..

The Importance of Low-Noise Reference Images

Figure 22 compares speckle-displacement data from the sidewall camera using the same wind-on image but different wind-off reference images. In Figure 22 (top), the reference image was “same-day”, acquired at the beginning of the shift with the rotor and LRTA in place. In Figure 22 (bottom) the reference image was acquired “post test,” after the rotor and LRTA had been removed. The RBOS measurement was far less noisy when the post-test image was used as the reference.

Uncertainty

The ability of RBOS to visualize vortices is limited by the smallest speckle displacements that can be detected. With image cross-correlation this becomes a question of how small a shift in the correlation peak can be measured. For noise-free data, this limit is about 0.1 pixels. With the addition of noise, the displacements must be larger.

The tell-tale signature of a vortex filament is a line toward which speckles on either side are displaced. The displacements, of opposite sign, are largest at points immediately to either side of the filament and quickly decrease to zero as distance from the filament increases. In the present test, peak-to-peak speckle displacements across a vortex filament as small as 0.25 pixels could be detected. Peak-to-peak displacements across the most visible filaments were almost always less than one pixel. The ability of the human to spatially integrate a scene and recognize patterns allowed vortex filaments to be identified in noisy data even when the speckle-displacements that defined the filaments were very small.

The principal source of uncertainty in determining the spatial coordinates of the vortex filaments was uncertainty in establishing their image-plane coordinates in the speckle-displacement distributions from each camera. The image-plane uncertainty depended on the SNR of the speckle-displacement distributions. SNR was highly variable and depended mostly on the test conditions. SNR increased with

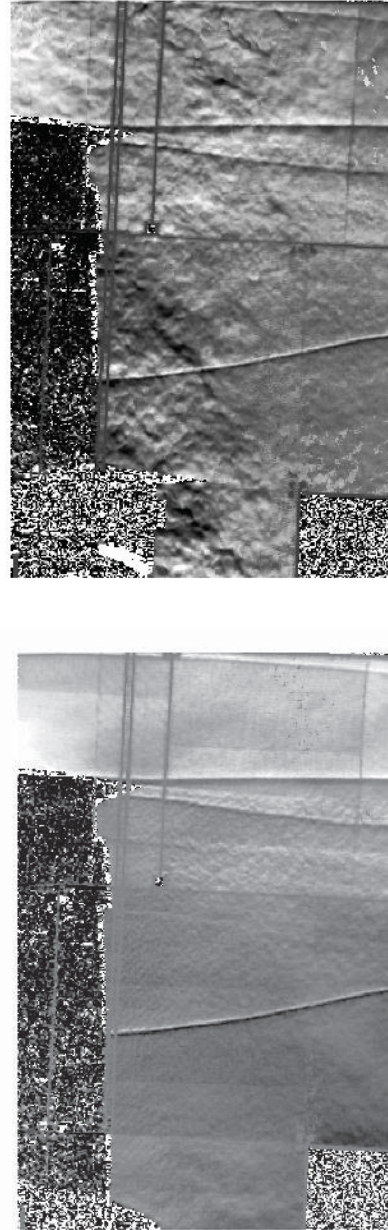


Figure 22. Speckle-displacement data from sidewall camera using same-day (top) and post-test (bottom) reference images ($\alpha = 0^\circ$, $\mu = 0.15$, $C_T / \sigma = 0.13$, $\psi = 5^\circ$).

increasing thrust coefficient and decreased with increasing advance ratio. The dependence on thrust coefficient is no surprise: higher thrust (lift) produces stronger vortices and thus a stronger signal (larger speckle displacements). The inverse relationship between SNR and advance ratio was also reported by Norman and Light (Ref. 8). They explained that bound circulation and vortex strength decline as advance ratio increases. This decrease occurs because more of the rotor lift at higher advance ratios is distributed on the forward and aft portions of the rotor disk.

The uncertainty in locating vortices in the speckle-displacement distributions also increased with vortex age: vortices from the most recent blade passage were usually significantly easier to detect than vortices from previous blade passages because the magnitudes of the vortex displacements were larger. The diameters of the vortex filaments did not appear to change (e.g., become larger and more diffuse) with vortex age (except in the region of distributed vorticity between the trim tab and the swept tip), so variations in diameters did not affect uncertainty.

The SNR in the speckle-displacement distributions from the sidewall camera was always significantly higher than for the ceiling camera. Since data from both cameras were required for a measurement, the measurement accuracies were limited by the ceiling camera. The lower SNR from the ceiling camera can be explained by its more complex optical path: reflections from two mirrors and a very oblique view through the window at the bottom of the light-fixture housing. Images may have been further degraded by spots of grease on the window that were discovered after the test when the periscope was removed. In contrast, the sidewall camera viewed the ROI directly. In addition, data from the ceiling camera were computed using the noisier same-day references that included heat convection currents from the model whereas data from the sidewall camera were computed using much less noisy post-test references. The ceiling camera was less affected by the heat convection currents compared to the sidewall camera because the ceiling camera line-of-sight did not pass directly over the model.

There were often significant variations in SNR from one cycle to the next in a sequence of images acquired at a constant test condition. The reasons for these variations are unknown.

Using the point and click method, the image coordinates of points on the most-clearly defined vortex filaments could be established with a uncertainty of no better than one pixel. For many vortices for which the visibility was very low, the uncertainty was much higher—perhaps 5–10 pixels. For uncorrelated uncertainties of 10 pixels, the theoretical uncertainty in the spatial coordinates of vortex points that appear in the images of both cameras is $\Delta x = 0.2$, $\Delta y = 1.0$, and $\Delta z = 0.3$ inches. The uncertainty is largest in the y direction, which is the predominant direction toward the cameras. Note that the dispersion of data in Figs 14, 15, and 19, 20 is larger in the y direction than the z direction.

The theoretical uncertainties were computed assuming that the correspondence of points between camera views had been accurately established by epipolar geometry. Errors in establishing this correspondence will appear as a mostly streamwise shift in the intersection between the largely vertical epipolar line and the largely horizontal vortex (Figure 10). When epipolar geometry was applied to known points in the fields of view of both cameras (e.g., the rotor tip trailing edge), the correspondence of points was within

the uncertainty due to image blur due to rotor motion (about 15 pixels, Figure 10). The spatial uncertainties scale approximately linearly with the image-plane uncertainties.

Another source of uncertainty in determining the spatial coordinates of vortices was uncertainty in the spatial coordinates of targets on the calibration structure that was used to compute the camera DLTs. The relative coordinates of these targets were not precisely known a priori, however their positions were refined as part of the calibration procedure. The absolute positions of the targets, and thus the vortices, relative to a fixed tunnel reference were known to within 2 or 3 inches. Measurements of the position of the trailing edge of the rotor tip agreed with the known radius of the rotor to within this uncertainty. Much smaller absolute uncertainties would have been possible if the calibration target coordinates had been measured in situ using theodolite or a photogrammetry system that had already been calibrated.

CONCLUSIONS

The spatial positions of vortex filaments near the tip of the advancing blade of a full-scale UH-60A rotor were successfully measured using RBOS to visualize the vortices and stereo photogrammetry to compute their positions. Vortex positions derived from the RBOS/photogrammetry measurements were in good agreement with PIV measurements for a case where both measurements were made. Vortices at the advancing blade station were observed to move upward and inboard as they aged. The apparent diameters of the vortex filaments did not increase with age. The visibility of the vortices in the RBOS data was greatest when the rotor thrust was high and the advance ratio was low. Vortices from all four rotor blades could be detected in cases where visibility was high. In cases where visibility was low, only the tip vortex produced by the most recent blade passage was evident. There were many cases in between, where two or three vortices could be identified. Visibility of vortices was much higher in data from the sidewall camera than the ceiling camera because of the much simpler optical path (no folding or mirrors). Therefore, more vortices were usually visible in data from the sidewall camera. Since data from both cameras were required for a measurement, the measurements were limited by the poorer visibility of data from the ceiling camera. The measurements were also limited by noise in the wind-off reference images, which were contaminated by heat convection currents from the model. This issue was resolved for the sidewall camera by using post-test reference images acquired after the model had been removed.

ACKNOWLEDGMENTS

This work was supported by the Experimental Capabilities Discipline of the Subsonic Rotary Wing Project (SRW Ex-Cap) of NASA's Fundamental Aeronautics Program. The authors thank Tom Norman of the Aeromechanics Branch at Ames for his encouragement and guidance during the test

and many useful suggestions afterwards. Thanks also to Alan Wadcock of the Aeromechanics Branch for helping to interpret the data and comparing it to PIV measurements. Thanks also to Gloria Yamauchi of the Aeromechanics Branch for her careful review of the paper. Louise Walker also contributed to the early phases of this project.

REFERENCES

- ¹Norman, T. R., Shinoda, P. M., Peterson, R. L., and Datta, A., "Full-Scale Wind Tunnel Test of the UH-60A Airloads Rotor," American Helicopter Society 67th Annual Forum, Virginia Beach, VA, May 2011.
- ²Barrows, D. A., Burner, A.W., Abrego, A.I., and Olson, L.E., "Blade Displacement Measurements of the Full-Scale UH-60A Airloads Rotor," AIAA Paper 2011-3655, 29th AIAA Applied Aerodynamics Conference, Honolulu, HI, June 2011.
- ³Abrego, A. I., Olson, L. E., Romander, E. A., Barrows, D. A., and Burner, A. W., "Blade Displacement Measurement Technique Applied to a Full-Scale Rotor Test," American Helicopter Society 68th Annual Forum, Fort Worth, TX, May 2012.
- ⁴Yamauchi, G. K., Wadcock, A. J., Johnson, W., and Ramasamy, M., "Wind Tunnel Measurements of Full-Scale UH-60A Tip Vortices," presented at the American Helicopter Society 68th Annual Forum, Ft. Worth, TX, May 2012.
- ⁵Wadcock, A.J., Yamauchi, G.K., Solis, E., Pete, A., "PIV Measurements in the Wake of a Full-Scale Rotor in Forward Flight," AIAA Paper 2011-370, 29th AIAA Applied Aerodynamics Conference, Honolulu, HI, June 2011.
- ⁶Heineck, J. T., Schairer, E. T., Kushner, L. K., and Walker, L. A., "Retroreflective Background Oriented Schlieren (RBOS) As Applied to Full-Scale UH-60 Blade Tip Vortices," American Helicopter Society Aeromechanics Specialists' Conference, San Francisco, CA, January 2010.
- ⁷Norman, T. R., Theodore, C., Shinoda, P. M., Fuerst, D., Arnold, U. T. P., Makinen, S., Lorber, P. M., O'Neill, J., "Full-Scale Wind Tunnel Test of a UH-60 Individual Blade Control System for Performance Improvement and Vibration, Loads, and Noise Control," American Helicopter Society 65th Annual Forum, Grapevine, TX, May 2009.
- ⁸Norman, T. R. and Light, J.S., "Rotor Tip Vortex Geometry Measurements Using Wide-Field Shadowgraph Technique," *Journal of the American Helicopter Society*, Vol. 32, No. 2, April 1987.
- ⁹Light, J.S., "Tip Vortex Geometry of a Hovering Helicopter Rotor in Ground Effect," *Journal of the American Helicopter Society*, Vol. 38, No. 2, April 1993.
- ¹⁰Norman, T. R. and Light, J.S., "Application of the Wide-Field Shadowgraph Technique to Rotor Wake Visualization," NASA TM 102222, October 1989.
- ¹¹Light, J.S., Swanson, A.A., and Norman, T.R., "Application of the Wide-Field Shadowgraph Technique to Helicopters in Forward Flight," *Journal of the American Helicopter Society*, Vol. 37, No. 2, April 1992, pp. 23–28.
- ¹²Swanson, A.A., and Light, J.S., "Shadowgraph Flow Visualization of Isolated Tiltrotor and Rotor/Wing Wakes," American Helicopter Society 48th Annual Forum, Washington, D.C., June 1992.
- ¹³Swanson, A.A., "Application of the Shadowgraph Flow Visualization Technique to a Full-Scale Helicopter Rotor in Hover and Forward Flight," paper AIAA 93-3411, 11th AIAA Applied Aerodynamics Conference, Monterey, CA, August 1993.
- ¹⁴Hargather, M.J., and Settles, G.S., "Retroreflective Shadowgraph Technique for Large-Scale Flow Visualization," *Applied Optics*, Vol. 48, No. 22, Aug. 2009, pp. 4449-4457.
- ¹⁵Parathasarathy, S. SP., Cho, Y. I., and Back, L. H., "Wide-Field Shadowgraph Flow Visualization of Tip Vortices Generated by a Helicopter Rotor," paper AIAA 85-1557, 18th AIAA Fluid Dynamics and Plasmadynamics and Lasers Conference, Cincinnati, OH, July 1985.
- ¹⁶Meyn, L.A., and Bennett, M.S., "Application of a Two Camera Video Imaging System to Three-Dimension Vortex Tracking in the 80 - by 120 - Foot Wind Tunnel," paper AIAA 93-3439, 11th AIAA Applied Aerodynamics Conference, Monterey, CA, August 1993.
- ¹⁷Klinge, F., Raffel, M., Hecklau, M., Kompenhans, J., and Gohmann, U., "Measurement of the position of rotor blade vortices generated by a helicopter in free-flight by means of the stereoscopic Background Oriented Schlieren Method (RBOS)," Paper number 22.6, 13th International Symposium on Application of Laser Techniques to Fluid Mechanics, Lisbon, Portugal, January 2006.
- ¹⁸Venkatakrishnan, L., and Meier, G. E. A., "Density Measurements Using the Background Oriented Schlieren Technique," *Experiments in Fluids* Vol. 37, 2004, pp. 237-247. DOI: 10.1007/S00348-004-0807-1.
- ¹⁹Raffel, M., Richard, H., and Meier, G.E.A., "On the applicability of background oriented optical tomography for large scale aerodynamic investigations," *Experiments in Fluids*, Vol. 28, No. 5, 2000, pp. 477–481.

- ²⁰Richard, H. and Raffel, M., "Principle and Applications of the Background Oriented Schlieren (BOS) Method," *Measurement Science and Technology*, Vol. 12, 2001, pp. 1576-15785.
- ²¹Raffel, M., Willert, C., and Kompenhans, J., *Particle Image Velocimetry, A Practical Guide*, Springer-Verlag, Berlin 1998.
- ²²Mikhail, E. M., *Introduction to Modern Photogrammetry*, John Wiley & Sons, Inc, New York, 2001.
- ²³Wolf, P.R., *Elements of Photogrammetry*, McGraw-Hill, New York, 1974.
- ²⁴Abdel-Aziz, Y.I., and Karara, H.M, "Direct Linear Transformation from Comparator Coordinates into Object-Space Coordinates," Proceedings of the Symposium on Close-Range Photogrammetry, Urbana, IL, January 1971.
- ²⁵Golub, G.H., and Reinsch, C., "Singular Value Decomposition and Least Squares Solutions," *Numer. Math.*, Vol. 14, pp. 403–420.
- ²⁶Press, W.H., Flannery, B.P, Teukolsky, S.A., and Vetterling, W.T., *Numerical Recipes*, Cambridge University Press, Cambridge, 1986, p 523.
- ²⁷Hartley, R., and Zisserman, A., "Epipolar Geometry and the Fundamental Matrix," *Multiple View Geometry In Computer Vision*, Cambridge University Press, Cambridge, UK, 2000.
- ²⁸Epipolar Geometry.svg – Wkipedia the free encyclopedia, Retrieved April 5, 2013 From http://commons.wikimedia.org/wiki/File:Epipolar_geometry.svg.
- ²⁹Hartley, R.I., "In Defense of the Eight-Point Algorithm," *IEEE Transactions on Pattern Analysis and Machine Intelligence*, Vol. 19, No. 6, pp. 580–593, October 1997.
- ³⁰Schairer, E.T., Heineck, J.T., Walker, S.M., and Yaste, D. M., "Predicting Camera Views for Image-Based Measurements in Wind Tunnels," AIAA Paper 2005-1349, presented at 43rd Aerospace Sciences Meeting and Exhibit, Reno, NV, January 2005.
- ³¹Kushner, L. K., and Schairer, E. T., "Planning Image-Based Measurements in Wind Tunnels by Virtual Imaging," paper AIAA 2011-930, 49th AIAA Aerospace Sciences Meeting including the New Horizons Forum and Aerospace Exposition, Orlando, FL, January 2011.
- ³²HPLS-692 DRAGON Series Data Sheet. Lightspeed Technologies. Retrieved January 18, 2012 from <http://www.light-speed-tech.com/documents/HPLS-692Series-2008-06-18.datasheet.pdf>.
- ³³Fleming, G. A., "RASP: Rotor Azimuth Synchronization Program (RASP) User's Guide, Version 1.3," NASA Langley Research Center, February 6, 2008.
- ³⁴Scotchlite™ Very High Gain Sheeting 3000X Retrieved 2010 from http://solutions.3m.com/wps/portal/3M/en_US/Manufacturing/Industry/Product-Catalog/Online-Catalog/?PC_7_RJH9U5230GE3E02LECFTDQGLE0000000_nid=J9JDL54MGVbeTRGGC52N4Mgl
- ³⁵Wadcock, A., Yamauchi, G., and Schairer, E., "Wind Tunnel Measurements of the Wake of a Full-scale UH-60A Rotor in Forward Flight," American Helicopter Society 69th Annual Forum, Phoenix, AZ, May 2013.